A Three-Step Method for Estimating Vortex Center Locations in Four-Dimensional Space from Radar-Observed Tornadic Mesocyclones

QIN XU

National Severe Storms Laboratory, Norman, Oklahoma

LI WEI

Cooperative Institute for Mesoscale Meteorological Studies, University of Oklahoma, Norman, Oklahoma

KANG NAI

National Severe Storms Laboratory, and Cooperative Institute for Mesoscale Meteorological Studies, University of Oklahoma, Norman, Oklahoma

(Manuscript received 10 July 2017, in final form 12 September 2017)

ABSTRACT

The recently developed two-dimensional variational methods for analyzing vortex winds from radar-observed mesocyclones can be extended to analyze three-dimensional vortex winds, but the first task for this extension is to estimate the vortex center location and its continuous variations in four-dimensional space so that the horizontal location of the vortex center can be expressed as a continuous function of height and time. To accomplish this task, a three-step method is developed in this paper. The method is applied to the Moore, Oklahoma, tornadic mesocyclone observed by the operational KTLX radar (Oklahoma City, Oklahoma) and the NSSL phased-array radar on 20 May 2013. The estimated vortex center trajectory at the ground level is verified with the tornado damage survey data. The estimated vortex center trajectories above the ground (up to 4-km height) reveal that the vortex core was initially tilted northeastward along the direction of the environmental flow and its vertical shear but became nearly vertical about 16 min later and 4 min before the vortex started to cause EF5 damages.

1. Introduction

The 3DVar system of Gao et al. (2013) can identify storm-scale midlevel circulations but cannot fully resolve the circulation as a result of the intrinsic limitation caused by the use of isotropic univariant background error covariance for analyzing each velocity component. The radar wind analysis system (RWAS) of Xu et al. (2015a) also cannot fully retrieve the circulation, especially the unobserved wind component tangential to the radar beam, because of the similar limitation caused by the use of isotropic background error covariance. To overcome the abovementioned limitation and to improve the mesocyclone wind analyses beyond the capabilities of the 3DVar and RWAS, a two-dimensional variational method was developed by formulating the background covariance with the desired vortex-flow dependences in a moving frame following the observed mesocyclone on each selected tilt of the radar scans (Xu et al. 2015b, hereinafter X15b).

In X15b, the mesocyclone vortex center moving velocity was estimated crudely by the time change of the vortex center location from the previous to the current volume scan, while the mesocyclone area and vortex center location were detected as by-products of the variational-analysis-based dealiasing (Xu et al. 2013) used in the RWAS, and the detected vortex center location was then used as a first guess and further estimated by applying the two-step algorithm (see section 3a of X15b) to the dealiased radial-velocity field in the mesocyclone area. To retrieve three-dimensional vortex winds from radar-observed mesocyclones, the previous two-dimensional variational method (X15b) should and can be extended with the background wind error correction functions formulated in a slantwise cylindrical coordinate system cocentered with the mesocyclone at each vertical level. For this extension, the horizontal

Corresponding author: Qin Xu, qin.xu@noaa.gov

DOI: 10.1175/JTECH-D-17-0123.1

location and moving velocity of the mesocyclone vortex center must be estimated first as continuous functions of height z and time t. To accomplish this, a three-step method is developed in this paper. The method is applied to the Moore, Oklahoma, tornadic mesocyclone observed by the operational KTLX radar (Oklahoma City, Oklahoma) and the NSSL phased-array radar (PAR; Zrnić et al. 2007) on 20 May 2013. Detailed techniques are presented for the three steps with the results obtained for the Moore tornadic mesocyclone in the next three sections. Conclusions follow in section 5.

2. Estimating vortex center location on each tilt of radar scan in step 1

In this step, the recently developed mesocyclone-targeted velocity dealiasing (Xu and Nai 2017) is used in addition to the variational-analysis-based dealiasing (Xu et al. 2013) to improve the dealiased data coverage over the mesocyclone area, and the vortex center location estimated as a by-product of the mesocyclone-targeted dealiasing is used as the first guess. After this, the vortex center location is estimated by applying the two-step algorithm (in section 3a of X15b) to the dealiased radial velocities over the mesocyclone area on each tilt of the radar scan. By transforming each estimated vortex center location from its radar coordinates to a common Cartesian coordinate system, a dataset of discrete vortex center locations is generated at irregularly distributed points in the two-dimensional space of (z, t).

The abovementioned procedure is applied to 10 and 22 consecutive volumes of dealiased radial velocities from the KTLX radar and PAR, respectively, over the period from 1951:42 to 2033:44 UTC for the Moore tornadic mesocyclone on 20 May 2013. This generates a dataset of M (= 319) vortex center locations between $0 < z \le 4$ km in the local Cartesian coordinate system centered at (35.2482°N, 97.6813°W) with $z = 0$ at the ground level of the PAR site. The horizontal location of the vortex center is denoted by $\mathbf{x}_c \equiv (x_c, y_c)$ in this coordinate system. The estimated value of $\mathbf{x}_c$ at the ith discrete data point, (z_i, t_i), in the abovementioned dataset is denoted by $\mathbf{x}_{ci} \equiv (x_{ci}, y_{ci})$. The dataset covers a time window of $0 \le t \le T$ (= 2522 s ≈ 42.03 min), which corresponds to the aforementioned period from 1951:42 to 2033:44 UTC. The two component values of $\mathbf{x}_{ci} \equiv (x_{ci}, y_{ci})$ estimated from the KTLX (or PAR) scan are shown in the unit of 0.1 km by the red (or green) integers, with their decimals rounded off for clarity, at the discrete points (z_i, t_i) in Figs. 1a and 1b, respectively.

3. Estimating $\mathbf{x}_c$ as a smooth function of (z, t) in step 2

In this step, $\mathbf{x}_c \equiv (x_c, y_c)$ is estimated as a smooth function of (z, t). This smooth function, denoted by $\mathbf{x}_c^b \equiv (x_c^b, y_c^b)$, is expressed by the following expansion of B-spline basis functions:

$$\mathbf{x}_c^b(z, t|\mathbf{a}_{kn\beta}) = \sum_{kn\beta} \mathbf{a}_{kn\beta} B_k(z) B_n^\beta(t), \tag{1}$$

where $\sum_{kn\beta}$ denotes the summation over k, n, and β; $\mathbf{a}_{kn\beta} \equiv (a_{kn\beta}, b_{kn\beta})$ is the vector coefficient associated with $B_k(z)$ $B_n^\beta(t)$ in the expansion, $B_k(z)$ denotes the linear basis function at the kth node point of z; and $B_n^\beta(t)$ denotes the cubic basis function of the βth order (with $\beta = 0, 1, 2$) at the nth node point of t. These B-spline basis functions are constructed similarly to those in section 6 of Xu (1989).

The coefficients $\mathbf{a}_{kn\beta}$ are determined by fitting the expression in (1) to $\mathbf{x}_{ci}$ $(1 \le i \le M)$. The vertical domain of $0 \le z \le H$ (= 4 km) is covered by a single element with the linear basis function. The time window of $0 \le t \le T$ is covered by a single element with the cubic basis functions. The fitting minimizes the following cost function:

$$J(\mathbf{a}_{kn\beta}) = \sum_i |\mathbf{x}_c^b(z_i, t_i|\mathbf{a}_{kn\beta}) - \mathbf{x}_{ci}|^2/M, \tag{2}$$

where $\sum_i$ denotes the summation over i from 1 to M and $\mathbf{x}_c^b(z_i, t_i \mid \mathbf{a}_{kn\beta})$ denotes the value of $\mathbf{x}_c^b(z, t \mid \mathbf{a}_{kn\beta})$ at (z_i, t_i).

Note that $\mathbf{v}_c^b(z, t) \equiv \partial_t \mathbf{x}_c^b(z, t)$ is the vortex center moving velocity derived from $\mathbf{x}_c^b(z, t)$. Using the cubic basis functions $B_n^\beta(t)$ to construct $\mathbf{x}_c^b(z, t)$ ensures $\mathbf{v}_c^b(z, t) \equiv \partial_t \mathbf{x}_c^b(z, t)$ to be not only continuous but also smooth in t. However, as the discrete data points of $\mathbf{x}_{ci}$ are confined within the time window of $0 \le t \le T$, the time derivative of $\mathbf{v}_c^b(z, t)$ may not be reliably estimated at and near the two node points of $t = 0$ and T. To reduce this uncertainty, $\partial_t \mathbf{v}_c^b(z, t) = \partial_t^2 \mathbf{x}_c^b(z, t)$ is constrained to zero at $t = 0$ and T. This constraint can be imposed simply by excluding the cubic basis function $B_n^\beta(t)$ for $\beta = 2$ in the constructed $\mathbf{x}_c^b(z, t)$, so the number of $\mathbf{a}_{kn\beta}$ used by the cost function in (2) is reduced from 12 to 8.

The estimated $x_c^b(z, t)$ $[y_c^b(z, t)]$ is shown by the dashed black counters in Fig. 1a (Fig. 1b). The trajectories of $\mathbf{x}_c^b(z, t)$ from $t = 0$ to T at the vertical levels of $z = 0, 1, 2$, 3, and 4 km are plotted by the blue, red, green, purple, and cyan curves, respectively, in Fig. 2a, where the red, green, purple and cyan plus (+) signs plot the data points of $\mathbf{x}_{ci}$ in the four vertical layers between $0 < z \le 1$ km, $1 < z \le 2$ km, $2 < z \le 3$ km, and $3 < z \le 4$ km, respectively. As shown, the trajectories of $\mathbf{x}_c^b(z, t)$ can capture the general trends but not the finescale variations of the vortex center location reflected by the discrete data of $\mathbf{x}_{ci}$. Since $\mathbf{x}_c^b(z, t \mid \mathbf{a}_{kn\beta})$ contains only eight vector coefficients, merely eight pairs of independent information are extracted by $\mathbf{x}_c^b(z, t)$ from the M (= 319) discrete data of $\mathbf{x}_{ci}$, and $\mathbf{x}_c^b(z, t)$ is inevitably too smooth to closely fit the discrete data of $\mathbf{x}_{ci}$. As shown in Fig. 1, the discrete data of $\mathbf{x}_{ci}$ are distributed nonuniformly and

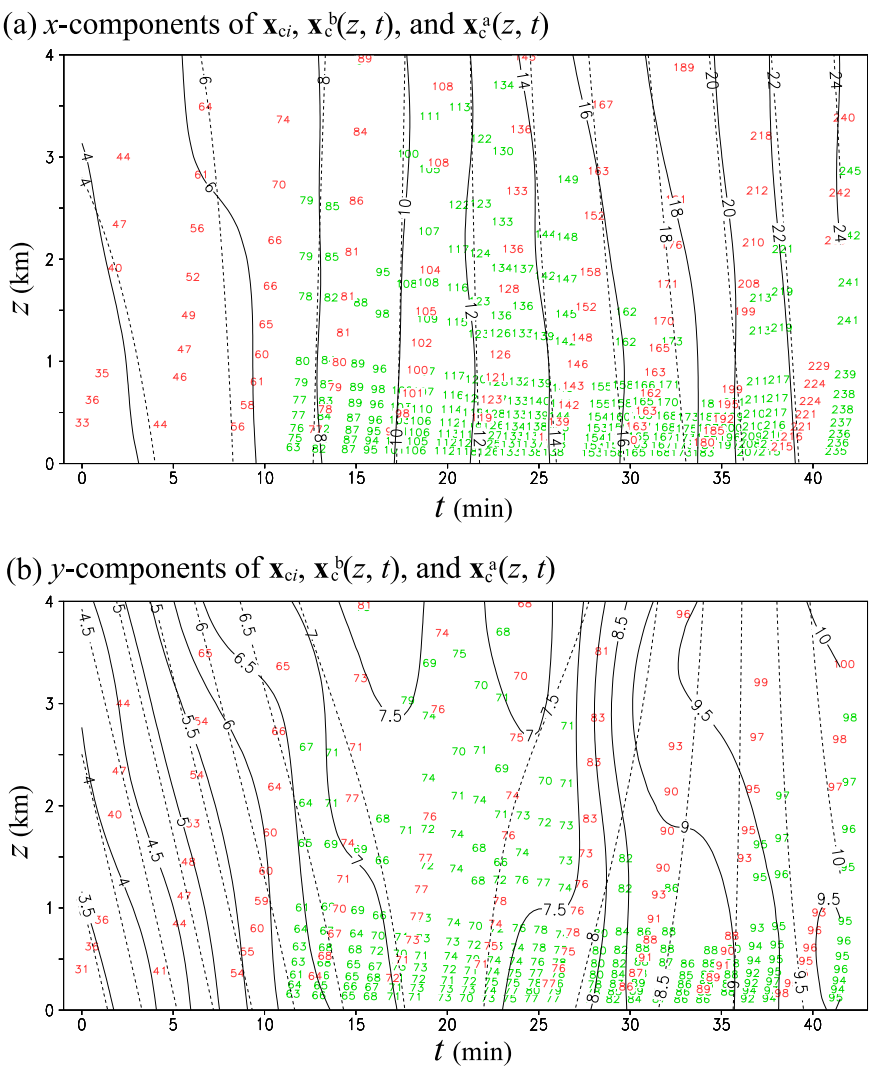

FIG. 1. (a) Estimated $x_c^b(z, t)$ plotted every 2 km (dashed black counters), $x_c^a(z, t)$ plotted every 2 km (solid black counters), and the estimated x_{ci} from KTLX (or PAR) scan displayed in the unit of 0.1 km by the red (or green) integers, to avoid cluttering, at discrete points (z_i, t_i) for $1 \le i \le M$. (b) As in (a), but for $y_c^b(z, t)$ and $y_c^a(z, t)$ plotted every 0.5 km, and for the estimated y_{ci} in the unit of 0.1 km. The local (x, y) coordinate system is centered at (35.2482°N, 97.6813°W), and the vertical coordinate origin ($z = 0$) is at the ground level of the PAR site. The time window of $0 \le t \le T =$ 2522 s (=42.03 min) corresponds to the period from 1951:42 to 2033:44 UTC. The vortex center detected first at $t = 0$ (on the 0.5° tilt) from the KTLX radar scan is at $(x, y) = (3.3, 3.1)$ km.

irregularly in (z, t). Because of this, the fit of $\mathbf{x}_c^b(z, t)$ to $\mathbf{x}_{ci}$ cannot be improved effectively by increasing the orders of the basis functions and/or enhancing the element resolutions (according to our additional experiments, not shown here). It is thus necessary to perform the third step of analysis with $\mathbf{x}_c^b(z, t)$ used as the background field as shown in the next section.

4. Further estimating $\mathbf{x}_c(z, t)$ in step 3

In this step, $\mathbf{x}_c(z, t)$ is further estimated in the form of $\mathbf{x}_c^a(z, t) \equiv \mathbf{x}_c^b(z, t) + \Delta\mathbf{x}_c(z, t)$, where $\Delta\mathbf{x}_c \equiv (\Delta x_c, \Delta y_c)$ is the incremental field obtained as a smooth function of (z, t) by applying a continuous version of statistical interpolation (see Daley 1991; section 5.4 of Bennett 1992) to the innovations defined by $\mathbf{d}_i \equiv \mathbf{x}_{ci} - \mathbf{x}_c^b(z_i, t_i)$ for $1 \le i \le M$. In this case, similar to the expression derived in (4.8) of Xu and Gong (2003), the incremental field can be expressed by

$$\Delta\mathbf{x}_c(z, t) = \sum_i \mathbf{c}_i C(z - z_i, t - t_i), \tag{3}$$

where $\mathbf{c}_i$ is the coefficient associated with the ith discrete data point at (z_i, t_i), $C(z, t)$ is the background error covariance function for each component of $\mathbf{x}_c^b(z, t)$, and the

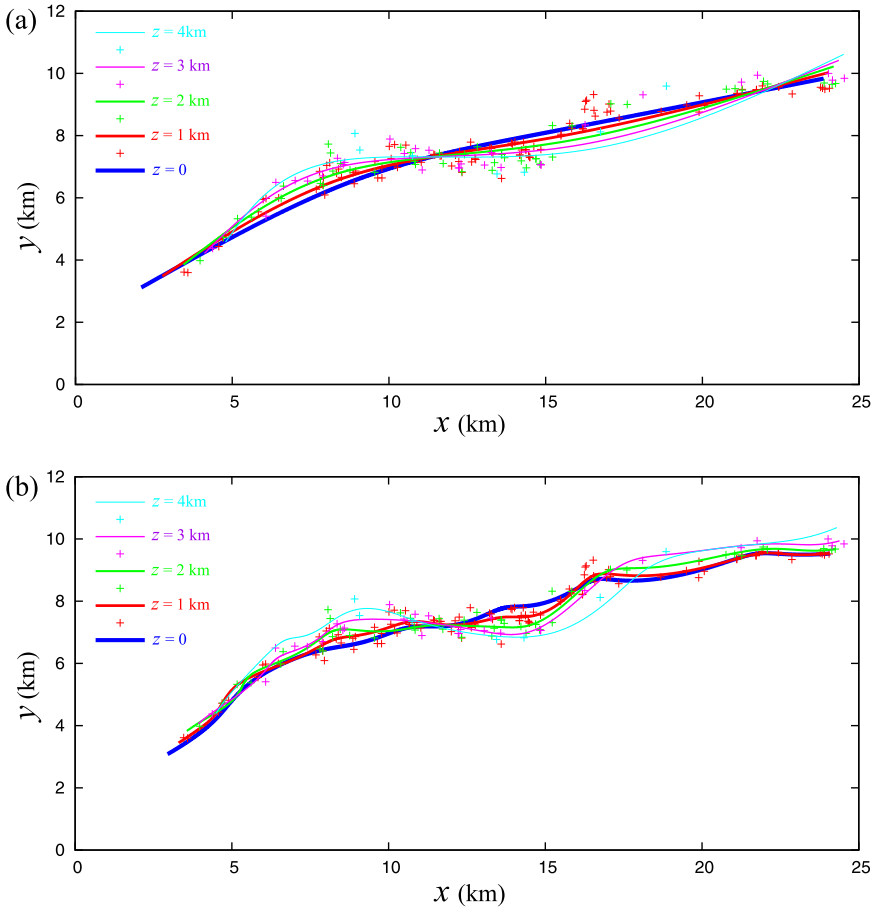

FIG. 2. (a) Trajectories of $\mathbf{x}_c^b(z, t)$ from $t = 0$ to T at $z = 0$, 1, 2, 3, and 4 km (blue, red, green, purple, and cyan curves, respectively), and data points of $\mathbf{x}_{ci}$ in the four vertical layers between $0 < z \le 1$ km, $1 < z \le 2$ km, $2 < z \le 3$ km, and $3 < z \le 4$ km (red, green, purple, and cyan + signs, respectively). (b) As in (a), but for trajectories of $\mathbf{x}_c^a(z, t)$ with the same data points of $\mathbf{x}_{ci}$.

errors for the two components of $\mathbf{x}_c^b(z, t)$ are assumed to be uncorrelated. The vector coefficients in (3) are solved from the following equation [see (4.9) of Xu and Gong 2003]:

$$(\mathbf{C}+\sigma_o^2\mathbf{I})(\mathbf{c}_1, \mathbf{c}_2, \ldots, \mathbf{c}_M)^{\mathrm{T}} = (\mathbf{d}_1, \mathbf{d}_2, \ldots, \mathbf{d}_M)^{\mathrm{T}}, \quad (4)$$

where $\mathbf{C}$ is the background error covariance matrix constructed in the M-dimensional data space with its ijth element given by $C(z_i - z_j, t_i - t_j)$, σ_o^2 is the error variance for each component of $\mathbf{x}_{ci}$ and is assumed to be a constant independent of i, $\mathbf{I}$ is the identity matrix in the M-dimension data space, and $()^{\mathrm{T}}$ denotes the transpose of ().

When the dataset of $\mathbf{x}_{ci}$ is generated from step 1, the accuracies of the two components of $\mathbf{x}_{ci}$ are limited intrinsically by the spatial resolution of radar radial-velocity observations, so σ_o can be estimated at least by $\Delta r/2$ (=0.125 km), where Δr is the range gate spacing of radar radial-velocity measurements. By assuming that the background error is uncorrelated with the data errors in $\mathbf{x}_{ci}$, the background error variance, denoted by σ_b^2 for each component of $\mathbf{x}_c^b(z, t)$, can be estimated by $\sigma_b^2 = \sigma_d^2 - \sigma_o^2$, where σ_d^2 is the variance for each component of $\mathbf{d}_i \equiv \mathbf{x}_{ci} - \mathbf{x}_c^b(z_i, t_i)$ and $2\sigma_d^2$ can be estimated by the minimum (=0.46^2 km^2) of the cost function in (2). This gives $\sigma_b = 0.3$ km. The background error covariance function is modeled by the following Gaussian function:

$$C(z, t) = \sigma_b^2 \exp(-z^2/2h^2 - t^2/2\tau^2), \quad (5)$$

where $h = 1$ km (or $\tau = 3$ min) is the decorrelation height (or time) scale specified empirically to filter data noises in $\mathbf{x}_{ci}$, but it resolves the finescale variations reflected by $\mathbf{x}_{ci}$. The resultant $\Delta\mathbf{x}_c(z, t)$ is rather insensitive to the variations of h within 1 ± 0.5 km and τ within 3 ± 1 min (not shown).

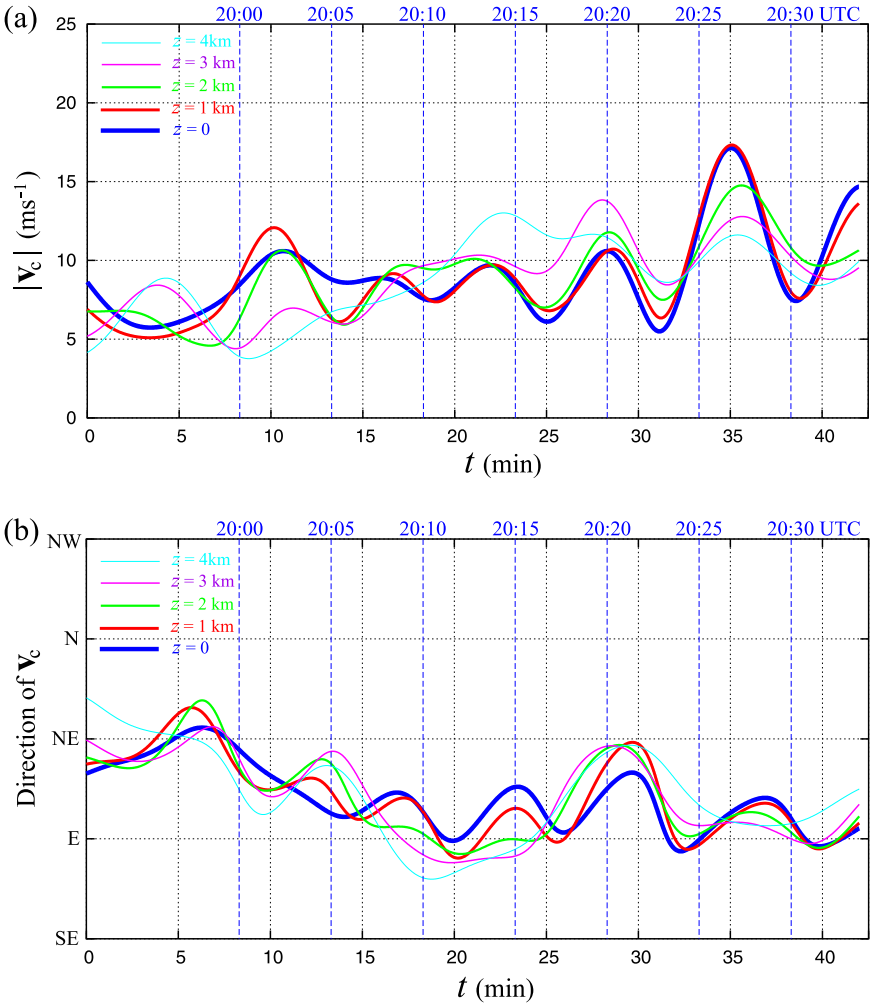

FIG. 3. (a) Absolute value $|\mathbf{v}_c|$ at $z = 0$, 1, 2, 3, and 4 km (blue, red, green, purple, and cyan curves, respectively). (b) As in (a), but for the direction of $\mathbf{v}_c$. The UTC time levels listed in blue on the top of each panel are denoted (blue dashed vertical lines).

The estimated $x_c^a(z, t)$ [or $y_c^a(z, t)$] is plotted by the solid black counters in Fig. 1a (Fig. 1b). These counters match the values of x_{ci} (or y_{ci}) more closely than the dashed contours of $x_c^b(z, t)$ [or $y_c^b(z, t)$]. The trajectories of $\mathbf{x}_c^a(z, t)$ at different vertical levels are plotted by the differently colored curves in Fig. 2b, similar to those in Fig. 2a. As these trajectories contain finescale variations, they fit the colored data points of $\mathbf{x}_{ci}$ in their respective adjacent vertical layers more closely than the trajectories of $\mathbf{x}_c^b(z, t)$ in Fig. 2a. The residual standard deviation for the misfit of $\mathbf{x}_c^a(z, t)$ to $\mathbf{x}_{ci}$ is 0.26 km, which is substantially smaller than that (of $\sqrt{2}\sigma_d = 0.46$ km) for the misfit of $\mathbf{x}_c^b(z, t)$ to $\mathbf{x}_{ci}$. The vortex center moving velocity is estimated by $\mathbf{v}_c = \partial_t \mathbf{x}_c^a$. The absolute value and direction of the estimated $\mathbf{v}_c$ are plotted as functions of t at different vertical levels in Figs. 3a and 3b, respectively.

The vertical variations of $\mathbf{x}_c^a(z, t)$ are shown at 11 uniformly divided time levels (from $t = 0$ to T) by the 11 color-segmented curves in Fig. 4, where each color-segmented curve is composed of four segments colored in red, green, purple, and cyan for $0 < z \le 1$ km, $1 < z \le 2$ km, $2 < z \le 3$ km and $3 < z \le 4$ km, respectively. As shown, the vertical profiles of $\mathbf{x}_c^a(z, t)$ at the first three time levels are highly slanted northeastward along the direction of the environmental flow and its vertical shear (see Fig. 7 of X15a). As t increases from $0.2T$ (1900:06.4 UTC) toward $0.5T$ (1912:48 UTC), the vertical profile of $\mathbf{x}_c^a(z, t)$ becomes gradually more upright with irregular variations and becomes nearly vertical at $t = 0.5T$ (1912:48 UTC), which is about 4 min before the vortex started to cause EF5 damages as shown by the tornado damage survey data (Burgess et al. 2014; Atkins et al. 2014) plotted in Fig. 4b. At the ground level ($z = 0$), the

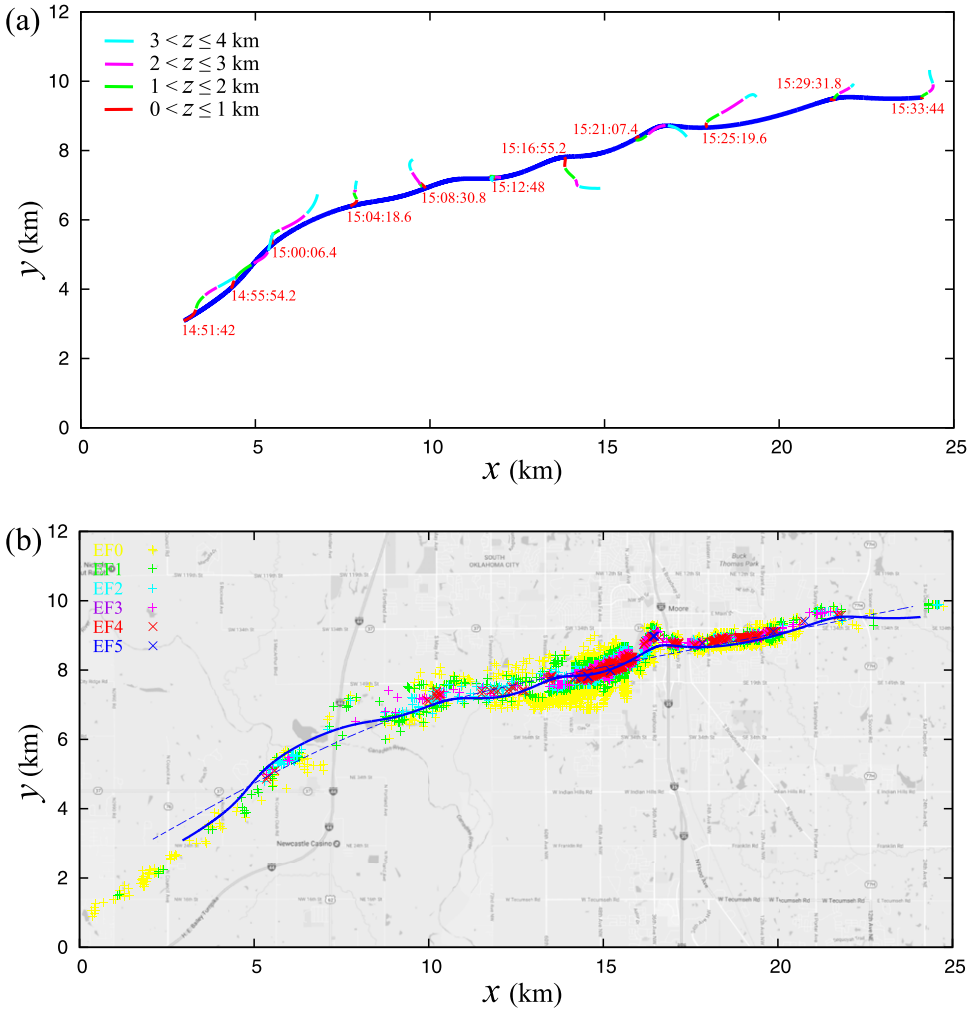

FIG. 4. (a) Vertical variations of $\mathbf{x}_c^a(z, t)$ at 11 uniformly divided time levels (with t increased incrementally every $0.1T$ from 0 to T, i.e., local time from 1451:42 to 1533:44) plotted by color-segmented curves atop the trajectory of $\mathbf{x}_c^a(0, t)$ (solid blue) that is reproduced here from that in Fig. 2b. Each color-segmented curve is composed of four segments [$0 < z \le 1$ km (red), $1 < z \le 2$ km (green), $2 < z \le 3$ km (purple), and $3 < z \le 4$ km (cyan)], and the corresponding local time is shown (red) for each color-segmented curve. (b) Trajectory of $\mathbf{x}_c^a(0, t)$ (solid blue curve), trajectory of $\mathbf{x}_c^b(0, t)$ (dashed blue curve), and tornado damage survey data points are plotted (atop a highway and Moore city street map printed in gray from Google Maps) by different colored symbols for different EF-scale damage ratings.

trajectory of $\mathbf{x}_c^a(0, t)$ plotted by the solid blue curve fits the damage survey data points (plotted by different colored symbols for different EF-scale damage ratings) much more closely than the trajectory of $\mathbf{x}_c^b(0, t)$ plotted by the dashed blue curve in Fig. 4b. However, since the temporal resolution of $\mathbf{x}_{ci}$ (even from the PAR scans) is limited to about 2 min, the trajectory of $\mathbf{x}_c^a(0, t)$ cannot capture the cusp in the damage path [0.5 km west of I-35 as shown in Fig. 5 of Burgess et al. (2014)] and the associated loop (about 0.5 km in total length) in the vortex track estimated from high-resolution radar scans (20 s per sweep on a single elevation) as shown in Fig. 11 of Kurdzo et al. (2015). For the same reason, the estimated $\mathbf{v}_c$ at $z = 0$ in Fig. 3 cannot capture the spiked time variations around 2022 UTC in Figs. 5c and 5d of Kurdzo et al. (2015).

5. Conclusions

A three-step method is developed in this paper to estimate the vortex center location of radar-observed mesocyclone in four-dimensional space with the estimated horizontal location of the vortex center, $\mathbf{x}_c \equiv (x_c, y_c)$, expressed as a continuous function of height and time.

The method is applied to the Moore, Oklahoma, tornadic mesocyclone observed by the operational KTLX radar and NSSL PAR on 20 May 2013. The trajectory of the estimated $\mathbf{x}_c$ at the ground level is verified with the tornado damage survey data (Burgess et al. 2014; Atkins et al. 2014). The trajectories of the estimated $\mathbf{x}_c$ above the ground reveal the vertical structure of the vortex core (up and limited to 4 km, as the radar scans used in this study intersected the vortex core too sparsely to reliably estimate $\mathbf{x}_c$ above 4 km) and its temporal variations, which can be used to further study the genesis and intensification of the tornado in this event. The method is computationally very efficient and can be used as a standalone not only after but also during the tornadic event in real time or nearly so. However, for nowcast applications, it is also necessary to retrieve three-dimensional vortex winds very efficiently in real time or nearly so, and this poses a challenging task for our continued study. Currently, the estimated $\mathbf{x}_c$ and $\mathbf{v}_c = \partial_t \mathbf{x}_c$ are being used to extend the two-dimensional variational method of X15b to retrieve three-dimensional vortex winds from radar-observed mesocyclones in four-dimensional space. The results will be reported in the near future.

Acknowledgments. The authors are thankful to Donald Burgess and Kiel Ortega for providing the damage survey data; to Pamela Heinselman, Pengfei Zhang and David Priegnitz for their help with the PAR data; and to Donald Burgess, James Kurdzo, and two anonymous reviewers for their constructive comments and suggestions. The research work was supported by the Warn-on-Forecast project at NSSL and the ONR Grants N000141410281 and N000141712375 to the University of Oklahoma (OU). Funding was also provided to CIMMS by NOAA/Office of Oceanic and Atmospheric Research under NOAA–OU Cooperative Agreement NA17RJ1227, U.S. Department of Commerce.

REFERENCES

Atkins, N. T., K. M. Butler, K. R. Flynn, and R. M. Wakimoto, 2014: An integrated damage, visual, and radar analysis of the 2013 Moore, Oklahoma, EF5 tornado. *Bull. Amer. Meteor. Soc.*, **95**, 1549–1561, doi:10.1175/BAMS-D-14-00033.1.

Bennett, A. F., 1992: *Inverse Methods in Physical Oceanography*. Cambridge University Press, 346 pp.

Burgess, D., and Coauthors, 2014: 20 May 2013 Moore, Oklahoma, tornado: Damage survey and analysis. *Wea. Forecasting*, **29**, 1229–1237, doi:10.1175/WAF-D-14-00039.1.

Daley, R., 1991: *Atmospheric Data Analysis.* Cambridge Atmospheric and Space Science Series, Vol. 2, Cambridge University Press, 457 pp.

Gao, J., and Coauthors, 2013: A real-time weather-adaptive 3DVAR analysis system for severe weather detections and warnings. *Wea. Forecasting*, **28**, 727–745, doi:10.1175/WAF-D-12-00093.1.

Kurdzo, J. M., D. J. Bodine, B. L. Cheong, and R. D. Palmer, 2015: High-temporal resolution polarimetric X-band Doppler radar observations of the 20 May 2013 Moore, Oklahoma, tornado. *Mon. Wea. Rev.*, **143**, 2711–2735, doi:10.1175/MWR-D-14-00357.1.

Xu, Q., 1989: Extended Sawyer–Eliassen equation for frontal circulations in the presence of small viscous moist symmetric stability. *J. Atmos. Sci.*, **46**, 2671–2683, doi:10.1175/1520-0469(1989)046<2671:ESEFFC>2.0.CO;2.

——, and J. Gong, 2003: Background error covariance functions for Doppler radial-wind analysis. *Quart. J. Roy. Meteor. Soc.*, **129**, 1703–1720, doi:10.1256/qj.02.129.

——, and K. Nai, 2017: Mesocyclone-targeted Doppler velocity dealiasing. *J. Atmos. Oceanic Technol.*, **34**, 841–853, doi:10.1175/JTECH-D-16-0170.1.

——, ——, S. Liu, C. Karstens, T. Smith, and Q. Zhao, 2013: Improved Doppler velocity dealiasing for radar data assimilation and storm-scale vortex detection. *Adv. Meteor.*, **2013**, 562386, doi:10.1155/2013/562386.

——, L. Wei, K. Nai, S. Liu, R. M. Rabin, and Q. Zhao, 2015a: A radar wind analysis system for nowcast applications. *Adv. Meteor.*, **2015**, 264515, doi:10.1155/2015/264515.

——, ——, and ——, 2015b: Analyzing vortex winds in radar-observed tornadic mesocyclones for nowcast applications. *Wea. Forecasting*, **30**, 1140–1157, doi:10.1175/WAF-D-15-0046.1.

Zrnić, D. S., and Coauthors, 2007: Agile-beam phased array radar for weather observations. *Bull. Amer. Meteor. Soc.*, **88**, 1753–1766, doi:10.1175/BAMS-88-11-1753.